ARTICLES
https://doi.org/10.1038/s41567-022-01702-z

nature physics

Check for updates

Correlated interlayer exciton insulator in heterostructures of monolayer WSe_2 and moiré WS_2/WSe_2

Zuocheng Zhang[1], Emma C. Regan[1,2,3], Danqing Wang[1,2,3], Wenyu Zhao[1], Shaoxin Wang[1], Mohammed Sayyad[4], Kentaro Yumigeta[4], Kenji Watanabe[5], Takashi Taniguchi[6], Sefaattin Tongay[4], Michael Crommie[1,3,7], Alex Zettl[1,3,7], Michael P. Zaletel[1,3] and Feng Wang[1,3,7] ✉

Moiré superlattices in van der Waals heterostructures have emerged as a powerful tool for engineering quantum phenomena. Here we report the observation of a correlated interlayer exciton insulator in a double-layer heterostructure composed of a WSe_2 monolayer and a WS_2/WSe_2 moiré bilayer that are separated by ultrathin hexagonal boron nitride. The moiré WS_2/WSe_2 bilayer features a Mott insulator state when the density of holes is one per moiré lattice site. When electrons are added to the Mott insulator in the WS_2/WSe_2 moiré bilayer and an equal number of holes are injected into the WSe_2 monolayer, a new interlayer exciton insulator emerges with the holes in the WSe_2 monolayer and the electrons in the doped Mott insulator bound together through interlayer Coulomb interactions. The interlayer exciton insulator is stable up to a critical hole density in the WSe_2 monolayer, beyond which the interlayer exciton dissociates. Our study highlights the opportunities for realizing quantum phases in double-layer moiré systems due to the interplay between the moiré flat band and strong interlayer electron interactions.

Excitonic insulators form when electrons and holes bind into pairs through an attractive Coulomb interaction[1,2]. The realization of excitonic insulators has been actively pursued for many decades[3]. The most striking observations of excitonic insulators are demonstrated in quantum Hall double layers[4–7], where Landau levels in a strong magnetic field are flat electronic bands that suppress the kinetic energy and enhance the electron–hole correlation. Flat electronic bands can also be achieved in moiré superlattices, which has enabled the observation of correlated insulators[8–14], superconductivity[9,11,14–16], Chern insulators[17–20], moiré excitons[21–24] and generalized Wigner crystal states[13,25] in different moiré heterostructures. By integrating the moiré superlattice into a double-layer system in which the moiré superlattice is separated from another semiconductor layer by an ultrathin hexagonal boron nitride (hBN) layer, we can simultaneously achieve a flat electronic band and strong interlayer electron–hole coupling. This interplay for moiré flat bands and strong interlayer electron–hole interactions can lead to novel correlated quantum phases, including excitonic insulators at zero magnetic field.

Here, we demonstrate a new type of correlated interlayer exciton insulator phases in a double-layer heterostructure composed of a WS_2/WSe_2 moiré bilayer strongly coupled to a WSe_2 monolayer that is separated by a 1-nm-thick hBN. A charge-neutral WSe_2 monolayer was used as a sensor to probe nearby Wigner crystal insulators in WS_2/WSe_2 heterostructures in ref. [25]. Our study explores the double-layer system where both the WSe_2 monolayer and the moiré heterostructure are doped with charge carriers that interact strongly with each other (Fig. 1a). The interlayer electron correlation leads to the formation of a new interlayer exciton insulator state composed of holes of a band insulator (in the WSe_2 monolayer) and electrons of a Mott insulator (in the WS_2/WSe_2 moiré bilayer). We utilize the delicate dependence of the 2s exciton resonance on the dielectric environment to determine the exciton insulating phase of the double-layer heterostructure[25]. At the same time, we track the charge distributions in the WSe_2 monolayer and the moiré bilayer using the trion state in the WSe_2 monolayer and the interlayer moiré exciton photoluminescence (PL) in the WS_2/WSe_2 moiré bilayer, respectively.

Figure 1a shows a schematic of a double-layer heterostructure device with both the top (V_t) and bottom (V_b) gates. The dual-gate configuration enables us to independently control the total hole concentration

$$p = -\frac{1}{e}\left[\frac{\varepsilon_0}{\frac{d_t}{\varepsilon_{hBN}}}(V_t - V_{t0}) + \frac{\varepsilon_0}{\frac{d_b}{\varepsilon_{hBN}} + \frac{d_m}{\varepsilon_{hBN}} + \frac{d_{WSe_2}}{\varepsilon_{WSe_2}}}(V_b - V_{b0})\right],$$

and the average vertical electric field

$$E = \frac{1}{2}\left(\frac{1}{d_b + d_m + d_{WSe_2}}V_b - \frac{1}{d_t}V_t\right),$$

where V_{t0} and V_{b0} are the onset gate voltages to inject holes into the moiré bilayer, d_b, d_m, d_{WSe_2} and d_t are the thickness of the bottom, middle, WSe_2 monolayer and top hBN dielectric layer, and ε_{hBN} is

[1]Department of Physics, University of California at Berkeley, Berkeley, CA, USA. [2]Graduate Group in Applied Science and Technolo gy, University of California at Berkeley, Berkeley, CA, USA. [3]Material Science Division, Lawrence Berkeley National Laboratory, Berkeley, CA, USA. [4]School for Engineering of Matter, Transport and Energy, Arizona State University, Tempe, AZ, USA. [5]Research Center for Functional Materials, National Institute for Materials Science, Tsukuba, Japan. [6]International Center for Materials Nanoarchitectonics, National Institute for Materials Science, Tsukuba, Japan. [7]Kavli Energy NanoSciences Institute, University of California Berkeley and Lawrence Berkeley National Laboratory, Berkeley, CA, USA.
✉e-mail: fengwang76@berkeley.edu

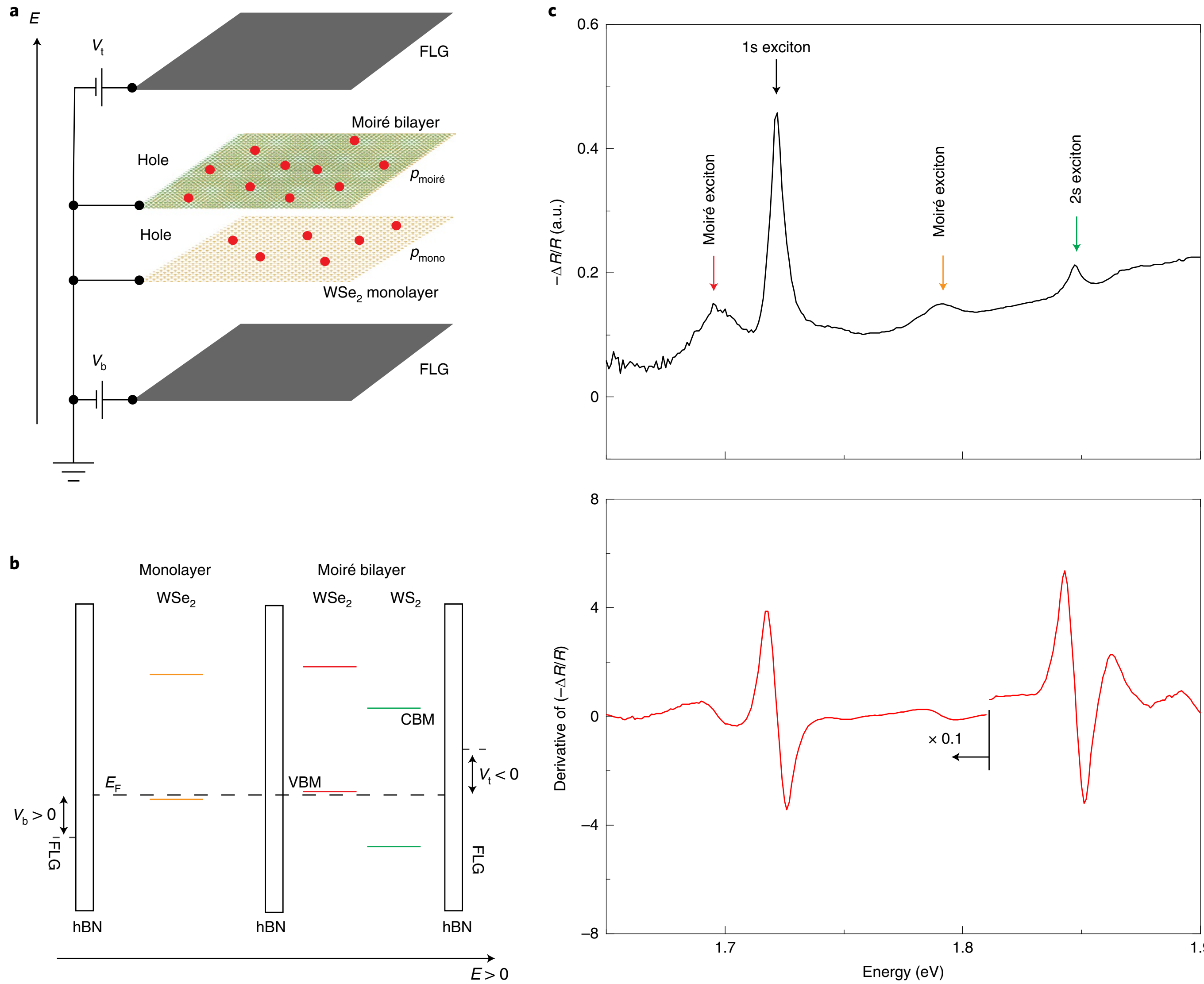

Fig. 1 | Schematic of double layers composed of a WS_2/WSe_2 moiré bilayer and WSe_2 monolayer. a, A schematic of the double-layer heterostructure with both the top and bottom gates. Both the moiré bilayer and the WSe_2 monolayer can be hole-doped in the system. These two layers are separated by an ultrathin hBN layer with thickness of approximately 1 nm. Thicker hBN layers are used for the gate dielectric layers. The electrical contacts to the TMDC flakes and the top/bottom gates are made of few-layer graphite (FLG). **b**, The band alignment of the three TMDC layers in the double layers. The conduction-band minimum (CBM) is in the moiré superlattice WS_2 layer. The valence-band maximum (VBM) can be in either the WSe_2 monolayer or the moiré superlattice WSe_2 layer, depending on the applied vertical electric field E. E_F is the Fermi energy. **c**, The broadband reflection spectrum (top) and the first-derivative reflection contrast spectrum (bottom) when both the moiré bilayer and the WSe_2 monolayer are charge neutral. The 1s and 2s exciton resonances of the WSe_2 monolayer and the moiré excitons of the WS_2/WSe_2 bilayer can be observed. The data of the first-derivative reflection contrast spectrum below 1.810 eV are multiplied by 0.1 for clarity.

the dielectric constant of hBN with $\varepsilon_{hBN} \approx 4.2$ (ref. [13]). The E field can change the relative potential of the WSe_2 monolayer and the WS_2/WSe_2 moiré bilayer, and consequently the distribution of the hole concentration in the WSe_2 monolayer (p_{mono}) and the WS_2/WSe_2 moiré bilayer ($p_{moiré}$). Figure 1b illustrates the band alignment of the three transition-metal dichalcogenide (TMDC) layers in the heterostructure. The conduction-band minimum of the WS_2 monolayer has much lower energy than that in WSe_2 monolayers. As a result, electrostatically doped electrons tend to be confined in the moiré superlattice WS_2 layer. On the other hand, holes can be distributed in either the WSe_2 monolayer or the moiré superlattice WSe_2 layer, depending on the E field: a positive E will shift holes to the moiré superlattice WSe_2 layer, while a negative E will prefer holes in the WSe_2 monolayer.

We utilize different excitonic features in the optical spectra to selectively probe the electron and hole doping in individual TMDC layers and the correlated insulator states. Three different devices have been studied (Extended Data Fig. 1), and they all exhibit similar behaviour. We focus on device I in the main text. Figure 1c shows a broadband reflection contrast spectrum (top panel) and corresponding first-derivative reflection contrast spectrum, $d(-\Delta R/R)/dE_{photon}$ (bottom panel) of the device with both the WSe_2 monolayer and the WS_2/WSe_2 moiré bilayer at charge neutrality. (All experimental measurements were performed at a nominal temperature of $T = 1.6$ K unless otherwise specified.) The two absorption peaks centred around 1.695 eV and 1.790 eV are moiré exciton resonances of the WS_2/WSe_2 moiré superlattice[23]. The strongest absorption peak, at around 1.722 eV, corresponds to the

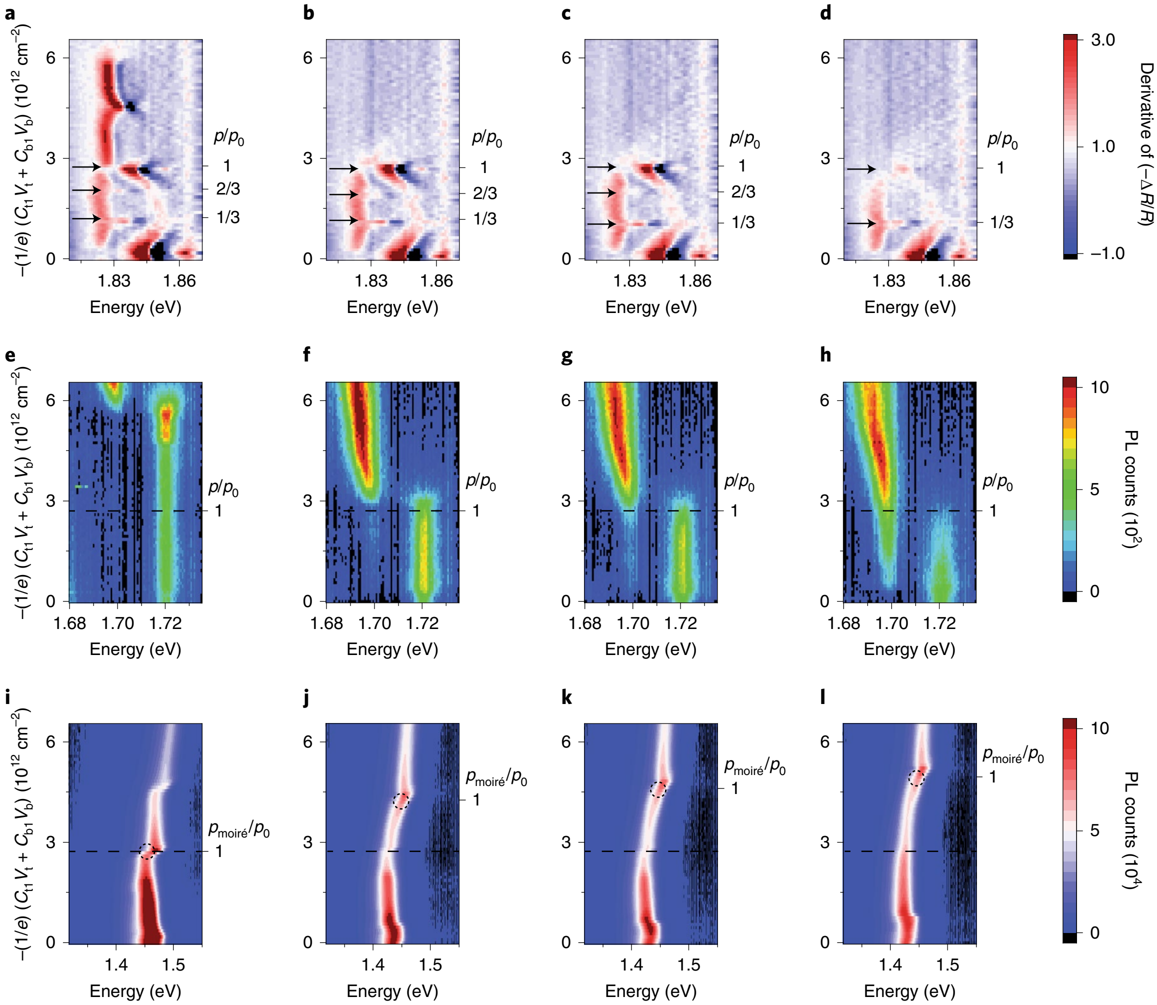

Fig. 2 | Correlated insulating states in double layers. a–l, Two-dimensional colour plots of derivative reflection contrast spectra and PL spectra in three different photon energy windows at E fields of 80 mV nm^{-1} (**a**, **e** and **i**), 8 mV nm^{-1} (**b**, **f** and **j**), 0 mV nm^{-1} (**e**, **g** and **k**) and −8 mV nm^{-1} (**d**, **h** and **l**), showing the derivative spectra of the WSe_2 monolayer 2s exciton to probe the correlated insulating state in the double-layer system (**a–d**), the WSe_2 monolayer 1s exciton and the trion PL spectra to probe the hole density in the WSe_2 monolayer (**e–h**) and the IX PL spectra of the WS_2/WSe_2 moiré bilayer to probe the hole density in the moiré bilayer (**i–l**), where the Mott insulator state in the moiré bilayer is characterized by an abrupt increase of the IX PL intensity and a blue shift of the IX energy. In **a**, the WSe_2 monolayer 2s exciton resonances at $p/p_0 = 1/3$, 2/3 and 1 correspond to the generalized Wigner crystal and Mott insulator states. In **e**, the WSe_2 monolayer is charge neutral with no trion PL signal. In **i**, the Mott insulator state occurs at $p_{moiré}/p_0 = 1$. In **b–d**, prominent 2s exciton resonances are still observed at $p/p_0 = 1$, indicating a correlated insulator state when the total doping is at one hole per moiré superlattice site. The trion PL starts to appear at $p/p_0 = 1$ in **f** and becomes increasingly stronger in **g** and **h**, showing that the correlated insulator has partial hole doping in the WSe_2 monolayer. In **j–l**, significantly higher total hole densities ($p/p_0 > 1$) are required to realize a filled moiré superlattice (that is, $p_{moiré}/p_0 = 1$), confirming that holes are now distributed in both the WSe_2 monolayer and the WS_2/WSe_2 moiré bilayer at $p/p_0 = 1$. The correlated insulators in **b–d** represent new interlayer exciton insulator states in the double-layer system.

1s exciton transition of the WSe_2 monolayer, which coincides with an additional weak moiré exciton state[23]. The other sharp transition at around 1.847 eV is from the 2s exciton transition of the WSe_2 monolayer. The 1s exciton resonance of the WSe_2 monolayer has a single peak with a narrow line width, comparable to that of isolated monolayers. The 2s exciton signal is more obvious in the derivative reflection contrast spectrum (Fig. 1c, lower).

We investigate the correlated interlayer electronic states by varying the gates' induced hole density

$$-\frac{1}{e}\left(C_{t1}V_t + C_{b1}V_b\right) = -\frac{1}{e}\left(\frac{\varepsilon_0}{\frac{d_t}{\varepsilon_{hBN}}}V_t + \frac{\varepsilon_0}{\frac{d_b}{\varepsilon_{hBN}} + \frac{d_m}{\varepsilon_{hBN}} + \frac{d_{WSe_2}}{\varepsilon_{WSe_2}}}V_b\right),$$

and the E field in the double-layer system. Figure 2 shows the two-dimensional colour plot of the derivative reflection contrast spectra and the PL spectra in three different photon energy windows (upper, middle and bottom panels) at an E field of 80 mV nm^{-1} (Fig. 2a,e,i), 8 mV nm^{-1} (Fig. 2b,f,j), 0 mV nm^{-1} (Fig. 2c,g,k) and −8 mV nm^{-1} (Fig. 2d,h,l). The upper panels (Fig. 2a–d) plot the first-derivative spectra of the WSe_2 monolayer 2s exciton resonance (with corresponding reflection contrast spectra in Extended Data Fig. 2) between 1.810 and 1.870 eV, which probes the correlated insulating state in the double-layer system due to its sensitivity to the dielectric screening in the system[25]. The middle panels (Fig. 2e–h) show the exciton and trion PL spectra of the WSe_2 monolayer between 1.680 to 1.735 eV (with background subtraction as documented in Supplementary Information Section 1), which probe the hole density in the WSe_2 monolayer. The lower panels (Fig. 2i–l) display the interlayer exciton (IX) PL spectra of the WS_2/WSe_2 moiré bilayer between 1.318 and 1.550 eV to probe the hole density in the moiré bilayer.

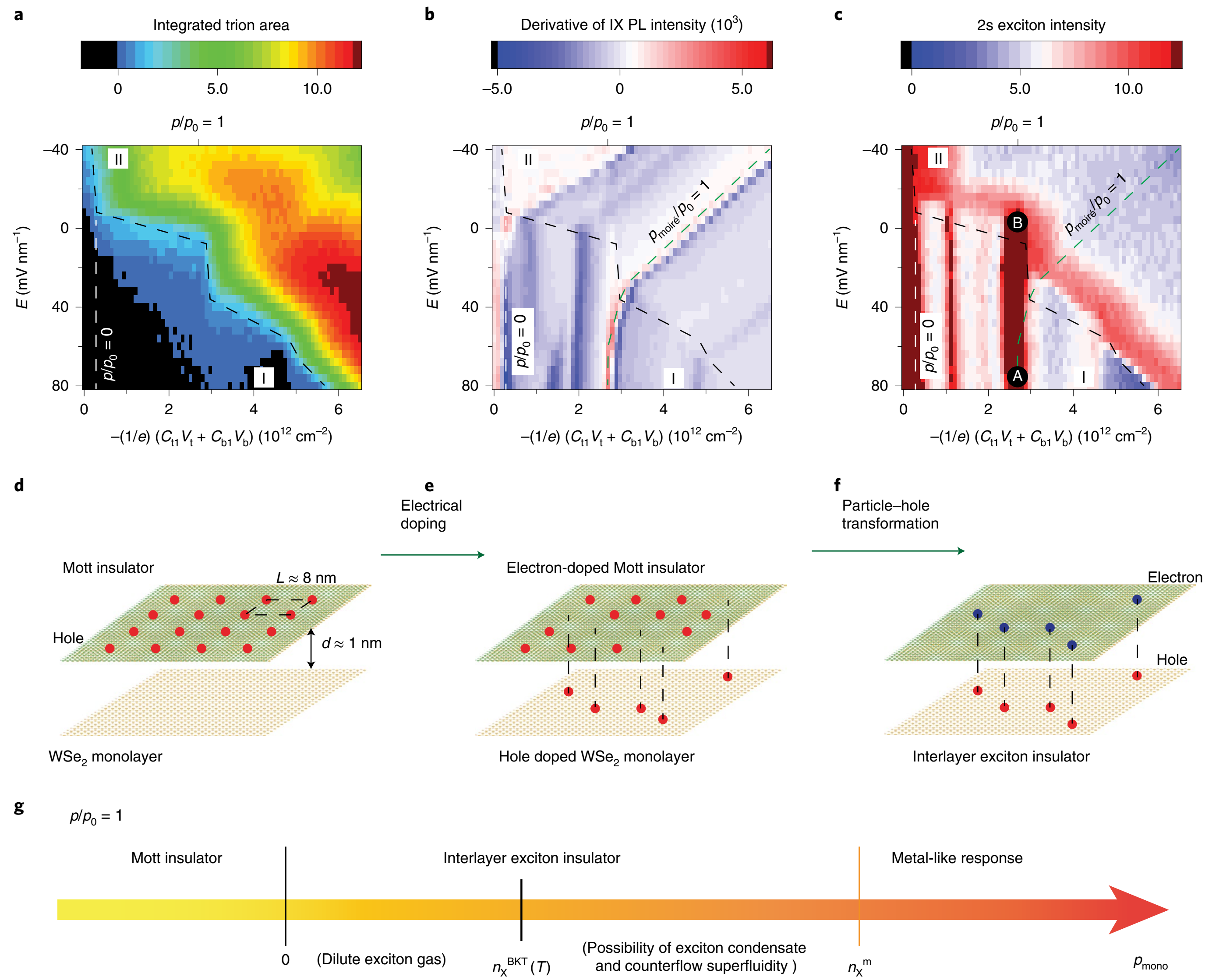

Fig. 3 | Phase diagram of the correlated interlayer exciton insulator. a, The WSe_2 monolayer integrated trion area as a function of $-\frac{1}{e}\left(C_{t1}V_t + C_{b1}V_b\right)$ and the E field. The dashed black line, determined by the emergence of the WSe_2 monolayer trion PL, separates region I (with a charge-neutral WSe_2 monolayer) from region II (with a hole-doped WSe_2 monolayer). The dashed white line corresponds to the charge-neutral line at $p/p_0 = 0$. **b**, The derivative of the IX PL intensity with respect to the gates' induced hole density $\mathrm{d}I_{IX}/\left[-\frac{1}{e}\left(C_{t1}V_t + C_{b1}V_b\right)\right]$. The Mott insulator state at $p_{moiré}/p_0 = 1$, characterized by a maximum $\mathrm{d}I_{IX}/\left[-\frac{1}{e}\left(C_{t1}V_t + C_{b1}V_b\right)\right]$ (dashed green line), coincides with the vertical line defining $p/p_0 = 1$ in region I. In region II, a higher total hole density p/p_0 is required to sustain the Mott insulator, confirming that an increasingly larger portion of holes is doped into the WSe_2 monolayer. **c**, The WSe_2 monolayer 2s exciton signal, which shows a stable correlated insulator state at $p/p_0 = 1$, extends region I to region II. The correlated insulator in region I, where $p_{mono} = 0$, corresponds to the Mott insulator in the moiré bilayer. The correlated insulator in region II represents a new correlated interlayer exciton insulator at a combined hole density of $p/p_0 = (p_{moiré} + p_{mono})/p_0 = 1$. **d**, The hole distribution of the Mott insulator at point A of **c**. **e**, The hole distribution of the interlayer correlated insulator with an effective 'one hole per moiré lattice site' at point B of **c**. The holes in the WSe_2 monolayer will avoid positions below the WS_2/WSe_2 moiré lattice site that is occupied by a hole owing to the strong interlayer Coulomb interaction. **f**, The particle–hole transformation of the doped Mott insulator state at point B of **c**. Electrons doped into the Mott insulator in the moiré layer spontaneously bind the holes doped into the WSe_2 monolayer to form the interlayer exciton insulator. **g**, Different correlated phases in the double layers as a function of p_{mono} at a fixed $p/p_0 = 1$.

Figure 2a shows the WSe_2 monolayer 2s exciton derivative spectra as a function of the gates' induced hole density $-\frac{1}{e}\left(C_{t1}V_t + C_{b1}V_b\right)$ at $E = 80\,\mathrm{mV\,nm^{-1}}$. The large positive E field confines doped holes in the moiré bilayer and keeps the WSe_2 monolayer charge neutral. Well-defined but red-shifted monolayer WSe_2 2s exciton resonances (Fig. 2a, arrows) can be observed at discrete doping levels of $p/p_0 = 1/3$, 2/3 and 1, where p_0 is estimated to be $(2.08 \pm 0.21) \times 10^{12}\,\mathrm{cm^{-2}}$ (see Supplementary Information Section 2 for details). These 2s exciton resonances result from reduced free-carrier screening and are signatures of correlated insulating states[25]. Since only the moiré heterostructure is doped with carriers at $E = 80\,\mathrm{mV\,nm^{-1}}$ for $p/p_0 < 2$, these correlated insulating states can be attributed to the known generalized Wigner crystal states at $p/p_0 = 1/3$ and 2/3, and the Mott insulator state at $p/p_0 = 1$ (refs. [13,25]). Figure 2e displays the PL spectra at the WSe_2 monolayer 1s exciton and trion transition energies. The 1s exciton PL is unchanged, and no trion PL is observed for $p/p_0 < 2$. These results confirm that the hole density is zero in the WSe_2 monolayer.

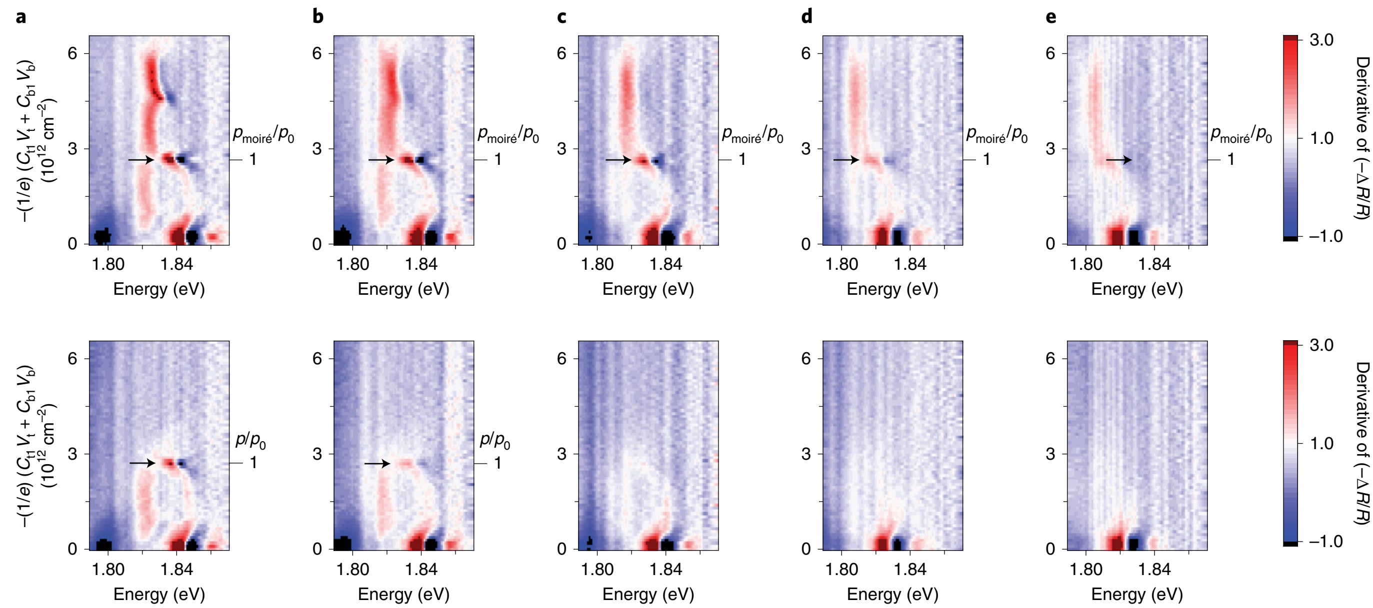

Fig. 4 | Temperature dependence of the Mott insulator and correlated interlayer exciton insulator. a–e, Correlated insulating states shown by the derivative spectra of the 2s exciton resonance in the WSe_2 monolayer at $E=80\,\mathrm{mV\,nm^{-1}}$ (upper) or $E=0\,\mathrm{V\,nm^{-1}}$ (lower) at $T=30\,\mathrm{K}$ (**a**), 60 K (**b**), 90 K (**c**), 120 K (**d**) and 150 K (**e**). The Mott insulator state, revealed by the 2s resonance at $p/p_0=p_{moiré}/p_0=1$ in the upper panel (arrows), persists up to 150 K. The correlated interlayer exciton insulator, revealed by the 2s resonance at $p/p_0=(p_{moiré}+p_{mono})/p_0=1$ in the lower panel (arrows), is stable up to 60 K.

Figure 2i displays the IX PL spectra of the WS_2/WSe_2 moiré bilayer. The IX PL shows a discrete change at $p/p_0=1$, where the PL resonance energy blue-shifts suddenly and the PL intensity exhibits a sudden increase. This coincides with the 2s exciton resonance at $p/p_0=1$ in Fig. 2a because all the doped holes are in the moiré bilayer with $p_{moiré}=p$ in this case. This abrupt increase in the IX PL intensity provides a reliable signature of the Mott insulating state with one hole at each moiré superlattice ($p_{moiré}/p_0=1$) (Extended Data Fig. 3 and refs. [12,26–28]).

Figure 2b shows that, at $E=8\,\mathrm{mV\,nm^{-1}}$, a prominent 2s exciton resonance is observed at $p/p_0=1$, indicating a correlated insulator state when the total doping is at one hole per moiré superlattice site. Clear trion PL can be observed at large hole density in Fig. 2f, accompanied by the suppression of the 1s exciton PL. This shows unambiguously that holes are now doped into the WSe_2 monolayer. In particular, the trion PL is present at $p=p_0$, indicating that the correlated insulator at $E=8\,\mathrm{mV\,nm^{-1}}$ already has partial hole doping in the WSe_2 monolayer. The binding energy of the hole-type trion is around 21 meV (Extended Data Fig. 4), which is consistent with the reported binding energy of the free hole-type trion in the WSe_2 monolayer[29–32]. The sudden change in the IX PL in Fig. 2j now takes place at $p/p_0>1$. This shows that a higher total hole density ($p/p_0>1$) is required to realize a filled moiré superlattice (that is, $p_{moiré}/p_0=1$), confirming that holes are now distributed in both the WSe_2 monolayer and the WS_2/WSe_2 moiré bilayer at $p/p_0=1$.

Figure 2c and 2d show corresponding data at $E=0$ and $E=-8\,\mathrm{mV\,nm^{-1}}$, respectively. The correlated insulator state can be observed in both Fig. 2c and 2d at total doping of $p/p_0=1$, although the corresponding 2s resonance becomes relatively weak at $E=-8\,\mathrm{mV\,nm^{-1}}$ in Fig. 2d. Significant hole doping of the WSe_2 monolayer is present in the $p/p_0=1$ correlated insulator state at $E=0\,\mathrm{mV\,nm^{-1}}$, as reflected in the appreciable WSe_2 trion PL signal at the dashed line in Fig. 2g. The hole doping in the WSe_2 monolayer becomes even stronger at $E=-8\,\mathrm{mV\,nm^{-1}}$ (Fig. 2h). At the same time, the IX PL spectra in Fig. 2k,l show that the moiré bilayer Mott insulator state ($p_{moiré}/p_0=1$), defined by the sudden change of the IX PL resonance, occurs at a total hole doping p that is much larger than p_0. At the correlated insulator state of $p/p_0=1$ (Fig. 2k,l, dashed lines), $p_{moiré}$ is smaller than p_0. These results provide independent evidence that both the WSe_2 monolayer and the WS_2/WSe_2 moiré bilayer are appreciably hole-doped when the full double-layer system is in the correlated insulator state ($p/p_0=1$) at $E=0$ and $E=-8\,\mathrm{mV\,nm^{-1}}$.

We map out the phase diagram of the new correlated insulating state at $p/p_0=1$ and different E fields in Fig. 3. Figure 3a shows the integrated trion area (probing the WSe_2 monolayer hole density) as a function of the gates' induced hole density $-\frac{1}{e}\left(C_{t1}V_t+C_{b1}V_b\right)$ and E field. The corresponding data for the derivative of the IX PL intensity $\mathrm{d}I_{IX}/\left[-\frac{1}{e}\left(C_{t1}V_t+C_{b1}V_b\right)\right]$ (probing the moiré bilayer hole density) and the 2s exciton signal (probing the correlated insulator state) are displayed in Fig. 3b and 3c, respectively.

The dashed white line in Fig. 3a–c defines $p/p_0=0$. The WSe_2 monolayer trion signal in Fig. 3a reveals two distinct regions for hole doping. The WSe_2 monolayer is charge neutral without any trion PL signal in region I (when the E field is below the dashed black line) but becomes hole-doped with a finite trion PL signal in region II (when the E field is above the dashed black line). The determination of the critical integrated trion area for hole doping in the WSe_2 monolayer is documented in Supplementary Information Section 3.

Figure 3b provides an independent determination of the Mott insulator state ($p_{moiré}/p_0=1$) in the moiré bilayer, as characterized by the sudden increase of the IX PL signal (that is, the maximum of $\mathrm{d}I_{IX}/\left[-\frac{1}{e}\left(C_{t1}V_t+C_{b1}V_b\right)\right]$ denoted by the dashed green line). The Mott insulator state ($p_{moiré}/p_0=1$) coincides with the vertical line defining $p/p_0=1$ in region I, as expected when the WSe_2 monolayer is charge neutral, and all the doped holes are in the moiré bilayer. However, in region II, the $p_{moiré}/p_0=1$ dashed line has a finite slope and persists to the highest doping density and negative E field. An increasingly higher total hole density p/p_0 is required to sustain the Mott insulator state ($p_{moiré}/p_0=1$) at more negative E field. This confirms that an increasingly larger portion of the holes is doped into the WSe_2 monolayer at positions deeper into region II. The WSe_2 monolayer 2s exciton signal in Fig. 3c probes the correlated insulating states of double layers. It shows that the correlated insulator state at $p/p_0 = 1$ can be stable in both region I and II. The correlated insulator in region I, where $p_{mono} = 0$, is defined by the Mott insulator phase in the WS_2/WSe_2 moiré bilayer. This insulator state extends into region II with the combined hole density defined by $p/p_0 = (p_{moiré} + p_{mono})/p_0 = 1$, and it eventually disappears at a large negative electric field (that is, sufficiently high p_{mono}). Similar phase diagrams are observed for all three devices (Extended Data Fig. 5).

Next, we compare the hole distribution at points A and B of Fig. 3c, where the total hole density is at $p/p_0 = 1$. The line cuts of the 2s exciton and trion spectra at these two points are shown in Extended Data Figs. 6 and 7. Figure 3d illustrates the hole distribution at point A, where the holes fill each moiré lattice site in the WS_2/WSe_2 moiré layer to form a Mott insulator. Figure 3e illustrates the hole distribution at point B, where finite hole density is present in both the top moiré bilayer and the bottom WSe_2 monolayer. The inhomogeneity in the hole doping in both the WSe_2 monolayer and the moiré bilayer is relatively small, as shown by the narrow phase boundary of the moiré bilayer Mott insulating state in Fig. 3b and the correlated insulator state in Fig. 3c. Therefore, the correlated insulator with distributed holes in both the WSe_2 monolayer and the moiré bilayer should be a new quantum phase that is relatively homogeneous. This new correlated interlayer insulator has total doping of 'one hole per moiré lattice site', but some of the holes are present in the WSe_2 monolayer and do not experience the moiré potential directly. This interlayer insulator is stabilized by the strong interlayer Coulomb interaction, which is around tens of meV in double-layer systems[33–37]. Because the moiré bilayer to monolayer distance of $d \approx 1$ nm is much smaller than the moiré length scale $L \approx 8$ nm, the interlayer Coulomb interaction can be extremely strong. This prevents the holes in the WSe_2 monolayer from occupying positions where the WS_2/WSe_2 moiré lattice site above already has a hole.

Figure 3f illustrates another perspective of this interlayer insulator by applying a particle–hole transformation relative to the Mott insulator state in the moiré bilayer. It clearly shows that electrons doped into the Mott insulator in the moiré bilayer can spontaneously bind the holes doped into the WSe_2 monolayer and form tightly bound interlayer excitons. Consequently, the insulating state at point B is described by an interlayer exciton insulator phase, where the interlayer exciton density n_X is the same as p_{mono}. This interlayer exciton insulator phase is stable up to an exciton density of $n_X \approx 0.50 p_0$ (Extended Data Fig. 8). When n_X is further increased, the interlayer excitons start to dissociate, and the interlayer exciton insulator dissolves into a phase that has a metal-like optical response.

The phase diagram in Fig. 3c shows that weaker insulating states are also present at $p/p_0 = 2/3$ and 1/3. These states are known as the generalized Wigner crystal states in region I. They also extend to a finite phase space in region II and can be understood as interlayer exciton insulators relative to the respective generalized Wigner crystal states in the moiré bilayer.

The interlayer excitons are bosons and can potentially form an exciton condensate at sufficiently low temperatures. A macroscopic two-dimensional exciton superfluid can be realized at the Berezinskii–Kosterlitz–Thouless (BKT) transition with n_X^{BKT} defined by $n_X^{BKT} = \frac{m_X k_B T}{1.3\hbar^2}$ (refs. [33–37]). Here, ħ is the reduced Planck constant, m_X is the exciton mass ($m_X = m_e + m_h$, with m_e and m_h the electron and hole mass), k_B is the Boltzmann constant and T is the temperature. Figure 3g illustrates the different correlated phases in the double layers as a function of p_{mono} at a fixed $p/p_0 = 1$. We start from the Mott insulator phase when $p_{mono} = 0$. The Mott insulator becomes an interlayer exciton insulator with finite exciton density $n_X = p_{mono} > 0$. Beyond a critical exciton density $n_X^m \approx 0.50 p_0$, the interlayer exciton insulator melts into a phase that has a metal-like optical response. Further experimental probes such as Coulomb drag and counterflow resistance measurements[5–7] will be needed to examine the possibility of exciton condensate and counterflow superfluidity (see Supplementary Information Section 4 for details). Many quantum phases could arise in such systems. For example, if the Mott insulator is a spin liquid, the correlated interlayer exciton insulator may carry new quantum excitations with fractionalized statistics[38,39].

Finally, we compare the temperature dependence of the Mott insulator and the correlated interlayer exciton insulator states. Figure 4 shows the 2s exciton transition probing the Mott insulator state (top panels, $E = 80$ mV nm^{-1}) and the correlated interlayer exciton insulator state (lower panels, $E = 0$ mV nm^{-1}) at $T = 30$ K (a), 60 K (b), 90 K (c), 120 K (d) and 150 K (e). The 2s exciton resonance intensity decreases monotonically as the temperature is increased. The 2s exciton resonance associated with the Mott insulator at $p_{moiré}/p_0 = 1$ can be observed up to $T = 150$ K (Fig. 4, upper panels). However, the 2s exciton resonance associated with the correlated insulator state at $p/p_0 = (p_{moiré} + p_{mono})/p_0 = 1$ disappears at a temperature above $T = 60$ K (Fig. 4, lower panels). This shows that the correlated interlayer exciton insulator state has a lower phase-transition temperature than the Mott insulator state. The difference between the Mott insulator and the correlated interlayer exciton insulator is summarized in Supplementary Information Section 5.

Online content

Any methods, additional references, Nature Research reporting summaries, source data, extended data, supplementary information, acknowledgements, peer review information; details of author contributions and competing interests; and statements of data and code availability are available at https://doi.org/10.1038/s41567-022-01702-z.

Received: 16 August 2021; Accepted: 29 June 2022;
Published online: 8 August 2022

References

1. Mott, N. F. The transition to the metallic state. *Philos. Mag. J. Theor. Exp. Appl. Phys.* **6**, 287–309 (1961).
2. HALPERIN, B. I. & RICE, T. M. Possible anomalies at a semimetal–semiconductor transistion. *Rev. Mod. Phys.* **40**, 755–766 (1968).
3. Kuneš, J. Excitonic condensation in systems of strongly correlated electrons. *J. Phys. Condens. Matter* **27**, 333201 (2015).
4. Eisenstein, J. P. Exciton condensation in bilayer quantum Hall systems. *Annu. Rev. Condens. Matter Phys.* **5**, 159–181 (2014).
5. Liu, X., Watanabe, K., Taniguchi, T., Halperin, B. I. & Kim, P. Quantum Hall drag of exciton condensate in graphene. *Nat. Phys.* **13**, 746–750 (2017).
6. Li, J. I. A., Taniguchi, T., Watanabe, K., Hone, J. & Dean, C. R. Excitonic superfluid phase in double bilayer graphene. *Nat. Phys.* **13**, 751–755 (2017).
7. Liu, X. et al. Crossover between strongly coupled and weakly coupled exciton superfluids. *Science* **375**, 205–209 (2022).
8. Cao, Y. et al. Correlated insulator behaviour at half-filling in magic-angle graphene superlattices. *Nature* **556**, 80–84 (2018).
9. Cao, Y. et al. Unconventional superconductivity in magic-angle graphene superlattices. *Nature* **556**, 43–50 (2018).
10. Chen, G. et al. Evidence of a gate-tunable Mott insulator in a trilayer graphene moiré superlattice. *Nat. Phys.* **15**, 237–241 (2019).
11. Chen, G. et al. Signatures of tunable superconductivity in a trilayer graphene moiré superlattice. *Nature* **572**, 215–219 (2019).
12. Tang, Y. et al. Simulation of Hubbard model physics in WSe_2/WS_2 moiré superlattices. *Nature* **579**, 353–358 (2020).
13. Regan, E. C. et al. Mott and generalized Wigner crystal states in WSe_2/WS_2 moiré superlattices. *Nature* **579**, 359–363 (2020).
14. Balents, L., Dean, C. R., Efetov, D. K. & Young, A. F. Superconductivity and strong correlations in moiré flat bands. *Nat. Phys.* **16**, 725–733 (2020).
15. Yankowitz, M. et al. Tuning superconductivity in twisted bilayer graphene. *Science* **363**, 1059–1064 (2019).
16. Lu, X. et al. Superconductors, orbital magnets and correlated states in magic-angle bilayer graphene. *Nature* **574**, 653–657 (2019).
17. Sharpe, A. L. et al. Emergent ferromagnetism near three-quarters filling in twisted bilayer graphene. *Science* **365**, 605–608 (2019).

18. Serlin, M. et al. Intrinsic quantized anomalous Hall effect in a moiré heterostructure. *Science* **367**, 900–903 (2020).
19. Chen, G. et al. Tunable correlated Chern insulator and ferromagnetism in a moiré superlattice. *Nature* **579**, 56–61 (2020).
20. Nuckolls, K. P. et al. Strongly correlated Chern insulators in magic-angle twisted bilayer graphene. *Nature* **588**, 610–615 (2020).
21. Seyler, K. L. et al. Signatures of moiré-trapped valley excitons in $MoSe_2/WSe_2$ heterobilayers. *Nature* **567**, 66–70 (2019).
22. Tran, K. et al. Evidence for moiré excitons in van der Waals heterostructures. *Nature* **567**, 71–75 (2019).
23. Jin, C. et al. Observation of moiré excitons in WSe_2/WS_2 heterostructure superlattices. *Nature* **567**, 76–80 (2019).
24. Alexeev, E. M. et al. Resonantly hybridized excitons in moiré superlattices in van der Waals heterostructures. *Nature* **567**, 81–86 (2019).
25. Xu, Y. et al. Correlated insulating states at fractional fillings of moiré superlattices. *Nature* **587**, 214–218 (2020).
26. Jin, C. et al. Stripe phases in WSe_2/WS_2 moiré superlattices. *Nat. Mater.* **20**, 940–944 (2021).
27. Miao, S. et al. Strong interaction between interlayer excitons and correlated electrons in WSe_2/WS_2 moiré superlattice. *Nat. Commun.* **12**, 3608 (2021).
28. Liu, E. et al. Excitonic and valley-polarization signatures of fractional correlated electronic phases in a WSe_2/WS_2 moiré superlattice. *Phys. Rev. Lett.* **127**, 037402 (2021).
29. Courtade, E. et al. Charged excitons in monolayer WSe_2: experiment and theory. *Phys. Rev. B* **96**, 085302 (2017).
30. Wang, G. et al. Colloquium: excitons in atomically thin transition metal dichalcogenides. *Rev. Mod. Phys.* **90**, 021001 (2018).
31. Li, Z. et al. Direct observation of gate-tunable dark trions in monolayer WSe_2. *Nano Lett.* **19**, 6886–6893 (2019).
32. Liu, E. et al. Gate tunable dark trions in monolayer WSe_2. *Phys. Rev. Lett.* **123**, 027401 (2019).
33. Perali, A., Neilson, D. & Hamilton, A. R. High-temperature superfluidity in double-bilayer graphene. *Phys. Rev. Lett.* **110**, 146803 (2013).
34. Fogler, M. M., Butov, L. V. & Novoselov, K. S. High-temperature superfluidity with indirect excitons in van der Waals heterostructures. *Nat. Commun.* **5**, 4555 (2014).
35. Wu, F.-C., Xue, F. & MacDonald, A. H. Theory of two-dimensional spatially indirect equilibrium exciton condensates. *Phys. Rev. B* **92**, 165121 (2015).
36. Conti, S., Neilson, D., Peeters, F. M. & Perali, A. Transition metal dichalcogenides as strategy for high temperature electron–hole superfluidity. *Condens. Matter* **5**, 22 (2020).
37. Conti, S., Van der Donck, M., Perali, A., Peeters, F. M. & Neilson, D. Doping-dependent switch from one- to two-component superfluidity in coupled electron–hole van der Waals heterostructures. *Phys. Rev. B* **101**, 220504 (2020).
38. Barkeshli, M., Nayak, C., Papić, Z., Young, A. & Zaletel, M. Topological exciton Fermi surfaces in two-component fractional quantized Hall insulators. *Phys. Rev. Lett.* **121**, 026603 (2018).
39. Hu, Y., Venderbos, J. W. F. & Kane, C. L. Fractional excitonic insulator. *Phys. Rev. Lett.* **121**, 126601 (2018).

Methods

Heterostructure preparation for optical measurements. All the two-dimensional flakes are first exfoliated from the bulk crystal on the SiO_2/Si substrate, and we stack them up using a polypropylene carbon-based dry transfer technology[40]. The moiré bilayer is composed of WS_2/WSe_2 heterostructures with a near-zero or 60° twist angle. The crystal orientations of these two flakes are determined optically using polarization-dependent second-harmonic generation measurements before the transfer process. The moiré bilayer and the WSe_2 monolayer are separated by an ultrathin hBN layer with a thickness of approximately 1 nm. These atomic double layers are contacted separately by FLG. The top and bottom gates are made of FLG, and two thicker hBN flakes serve as the top and bottom dielectric layers with dielectric constant of $\varepsilon_{hBN} \approx 4.2 \pm 0.4$ (ref. [13]). The heterostructure is further capped by an hBN flake to ensure the cleanness of the top graphite and aid in the device assembly. Finally, the whole stack is released onto a 90 nm SiO_2/Si substrate. Electrodes (5 nm Cr/100 nm Au) are defined by using a standard photolithography system (Durham Magneto Optics, MicroWriter) and an e-beam deposition system. The top and bottom gate voltages are applied by using Keithley 2400 or 2450 source meters. The WSe_2 monolayer, moiré bilayer and heavily hole-doped Si are grounded during the measurements.

Optical measurements. The optical measurements are performed in a cryostat with a temperature down to $T = 1.6$ K (Quantum Design, Opticool). We use diode lasers as the light source for reflection spectroscopy. The light is focused on the sample by a 20× Mitutoyo objective with ~2 µm beam size. The reflected light is collected by the same objective and dispersed by a spectrometer before reaching the camera. We take three spectra to get the reflection contrast spectrum: a spectrum on the sample (R_s), a spectrum without the sample (R_{ref}) and a background spectrum (R_{bkg}). The reflection contrast ($-\Delta R/R$) is calculated as $-(R_s - R_{ref})/(R_{ref} - R_{bkg})$. The noise level is ~0.1% in our measurements.

PL measurements are performed using a 532 nm continuous laser source, which is spectrally filtered by a 650 nm short-pass filter. The excitation light is focused on the sample by a 20× Mitutoyo objective with ~2 µm beam size and then filtered out by a 700 nm long-pass filter. The PL is collected and analysed with a monochromator and a camera. The excitation power is around 2 µW, and the integration time is 1 min.

Estimation of the critical interlayer exciton density. The point at the critical interlayer exciton density n_X is labelled as point X in Extended Data Fig. 8, beyond which the correlated interlayer exciton dissolves into a phase that has a metal-like optical response. We estimate the hole density in the WSe_2 monolayer (p_{mono}) at point X through the trion PL intensity. Different double-layer configurations with the same trion PL intensity will have approximately the same p_{mono} because the trion PL emission is dominated by holes in the WSe_2 monolayer only. The dashed blue line in Extended Data Fig. 8a denotes states with the same trion PL intensity as, and therefore similar p_{mono} to, the X point.

The dashed green line in Extended Data Fig. 8b corresponds to the Mott insulator in the moiré bilayer ($p_{moiré}/p_0 = 1$), which is determined by the maximum of $\mathrm{d}I_{IX}/\left[-\frac{1}{e}\left(C_{t1}V_t + C_{b1}V_b\right)\right]$. The carrier density in the WSe_2 monolayer p_{mono} along this dashed green line can be calculated as $p_{mono} = p - p_{moiré}$. The intersection of the dashed blue line and the dashed green line in Extended Data Fig. 8c is at around $p/p_0 = 1.5$. The hole density in the WSe_2 monolayer is $p_{mono} = p - p_{moiré} = 1.5p_0 - p_0 = 0.5p_0$ at the intersection. Point X should have a similar p_{mono} because it has the same trion intensity. Consequently, we estimate the critical interlayer exciton density at point X to be $n_X = p_{mono} \approx 0.5p_0$.

Data availability

Source data are provided with this paper.

References

40. Wang, L. et al. One-dimensional electrical contact to a two-dimensional material. *Science* **342**, 614–617 (2013).

Acknowledgements

This work was supported primarily by the U.S. Department of Energy, Office of Science, Office of Basic Energy Sciences, Materials Sciences and Engineering Division under contract no. DE-AC02-05-CH11231 (van der Waals heterostructures programme, KCWF16). The device fabrication was also supported by the U.S. Army Research Office under MURI award W911NF-17-1-0312. E.C.R. acknowledges support from the Department of Defense through the National Defense Science and Engineering Graduate Fellowship (NDSEG) Program. S.T. acknowledges support from DOE-SC0020653, NSF CMMI 1933214, NSF mid-scale 1935994, NSF 1904716, NSF DMR 1552220 and DMR 1955889. K.W. and T.T. acknowledge support from the Elemental Strategy Initiative conducted by the MEXT, Japan, grant no. PMXP0112101001, JSPS KAKENHI grant no. JP20H00354 and the CREST(JPMJCR15F3), JST.

Author contributions

F.W. conceived the research. Z.Z. fabricated the device and performed most of the experimental measurements. E.C.R., D.W. and W.Z. contributed to the optical measurements. Z.Z. and F.W. performed data analysis. E.C.R., D.W., W.Z., S.W., M.C. and A.Z. contributed to the fabrication of van der Waals heterostructures. M.P.Z. contributed to the theory. M.S., K.Y. and S.T. grew WSe_2 and WS_2 crystals. K.W. and T.T. grew hBN crystals. All authors discussed the results and wrote the manuscript.

Competing interests

The authors declare no competing interests.

Additional information

Extended data is available for this paper at https://doi.org/10.1038/s41567-022-01702-z.

Supplementary information The online version contains supplementary material available at https://doi.org/10.1038/s41567-022-01702-z.

Correspondence and requests for materials should be addressed to Feng Wang.

Peer review information *Nature Physics* thanks Andrea Perali and the other, anonymous, reviewer(s) for their contribution to the peer review of this work.

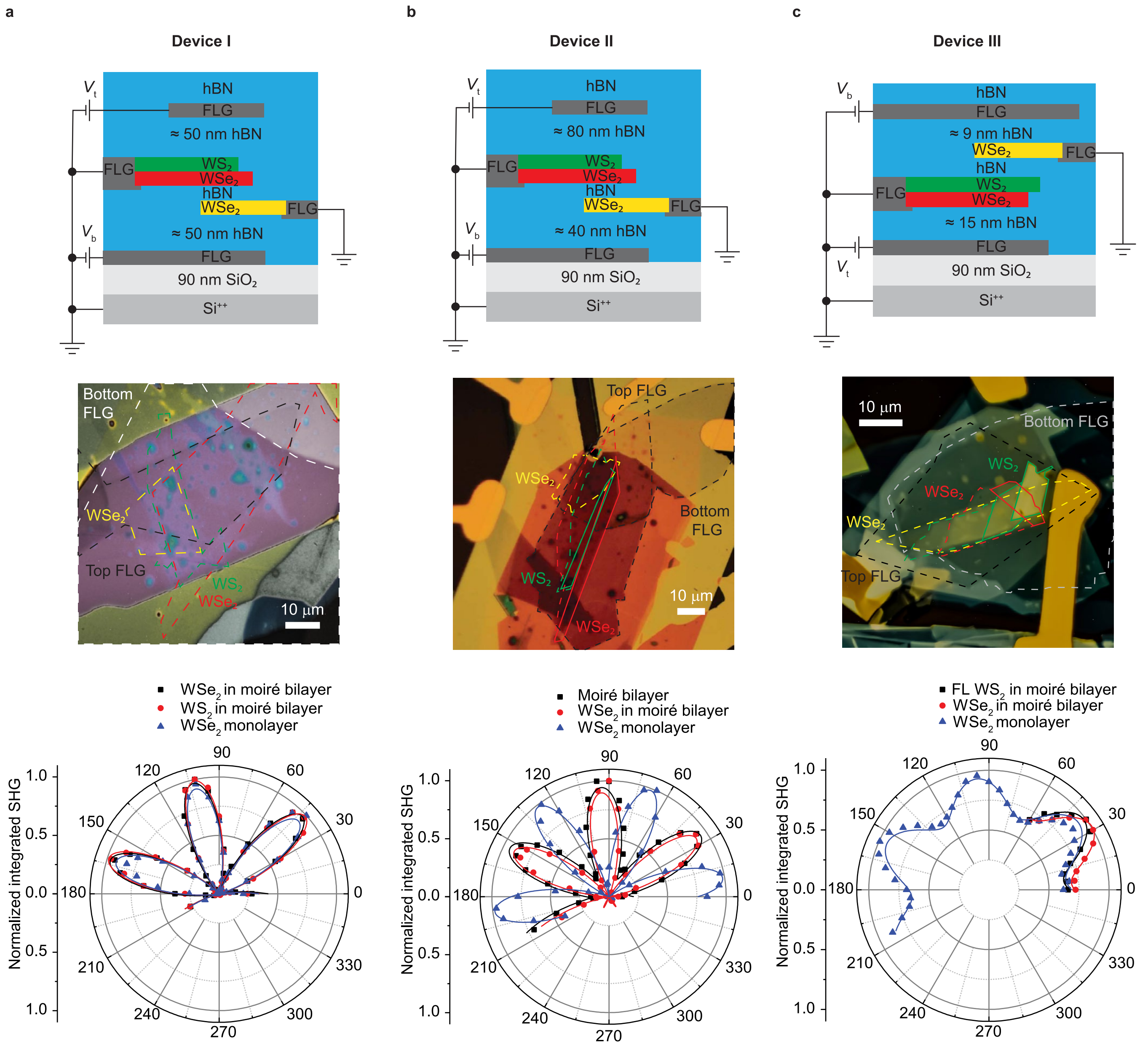

Extended Data Fig. 1 | Device information. a–c, Three side-view schematics, optical microscope images, and second harmonic generation (SHG) results of Device I (**a**), Device II (**b**), and Device III (**c**). **a**, The top (bottom) hBN thickness is approximately 50 nm (50 nm). The stack is capped with an approximately 65 nm thick hBN layer. In the optical microscopy image, the dashed green (red) line outlines the WS_2 (WSe_2) layer in the moiré heterostructure, the dashed yellow line outlines the WSe_2 monolayer, the dashed black (white) line outlines the top (bottom) FLG gate. These three flakes are aligned, as demonstrated by the SHG signal. The moiré bilayer has a near-60º twist angle. **b**, The top (bottom) hBN thickness is approximately 80 nm (40 nm). The stack is capped with an approximately 55 nm thick hBN layer. In the optical microscopy image, the dashed green (red) line outlines the WS_2 (WSe_2) layer in the moiré heterostructure, the dashed yellow line outlines the monolayer WSe_2, and the dashed black line outlines the top and bottom FLG gate. The solid lines correspond to a few-layer TMDCs that are attached to the monolayers. The twist angle between the moiré bilayer and the WSe_2 monolayer is around 25 degrees. The moiré bilayer has a near-zero twist angle as it shows an enhanced SHG signal. **c**, The stacking order of Device III is opposite to that in Device I and Device II. The moiré bilayer in device III is below the WSe_2 monolayer. The top (bottom) hBN thickness is approximately 9 nm (15 nm). The stack is further capped with an approximately 8 nm thick hBN layer. In the optical microscopy image, the dashed green (red) line outlines the WS_2 (WSe_2) layer in the moiré heterostructure, the dashed yellow line outlines the monolayer WSe_2, the dashed black (white) line outlines the top (bottom) FLG gate. The solid lines correspond to a few-layer TMDCs that are attached to the monolayers. These three layers are aligned, as determined by the SHG measurements. The moiré bilayer in device III has a near-zero twist angle.

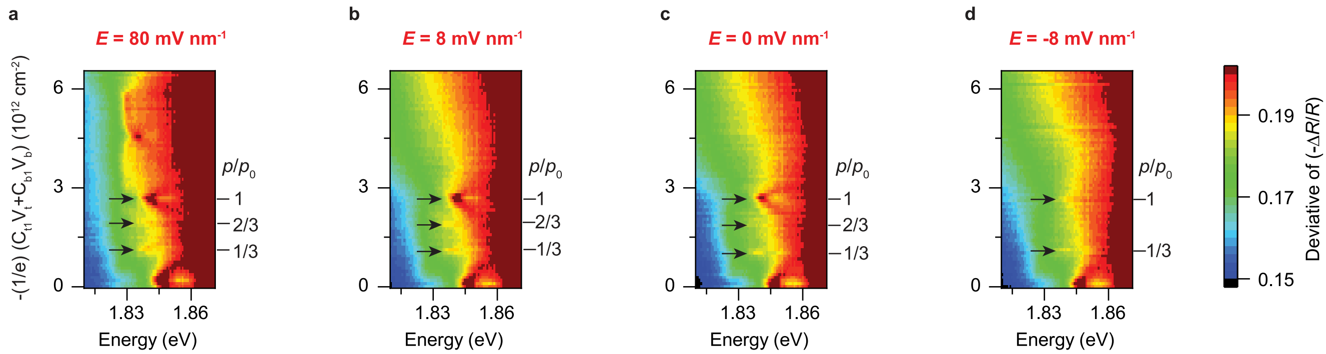

Extended Data Fig. 2 | Reflection contrast spectra of 2s exciton at four representative vertical electric fields. a–d, The two-dimensional color plots of reflection contrast spectra at the E field of 80 mV nm^{-1} (**a**), 8 mV nm^{-1} (**b**), 0 mV nm^{-1} (**c**), and −8 mV nm^{-1} (**d**). The monolayer WSe_2 2s exciton resonances at $p/p_0 = 1/3$, 2/3, and 1 in **a** correspond to the generalized Wigner crystal and Mott insulator states. Prominent 2s exciton resonances are still observed at $p/p_0 = 1$ in **b**–**d**, indicating a correlated insulating state when the total doping is at one hole per moiré superlattice site.

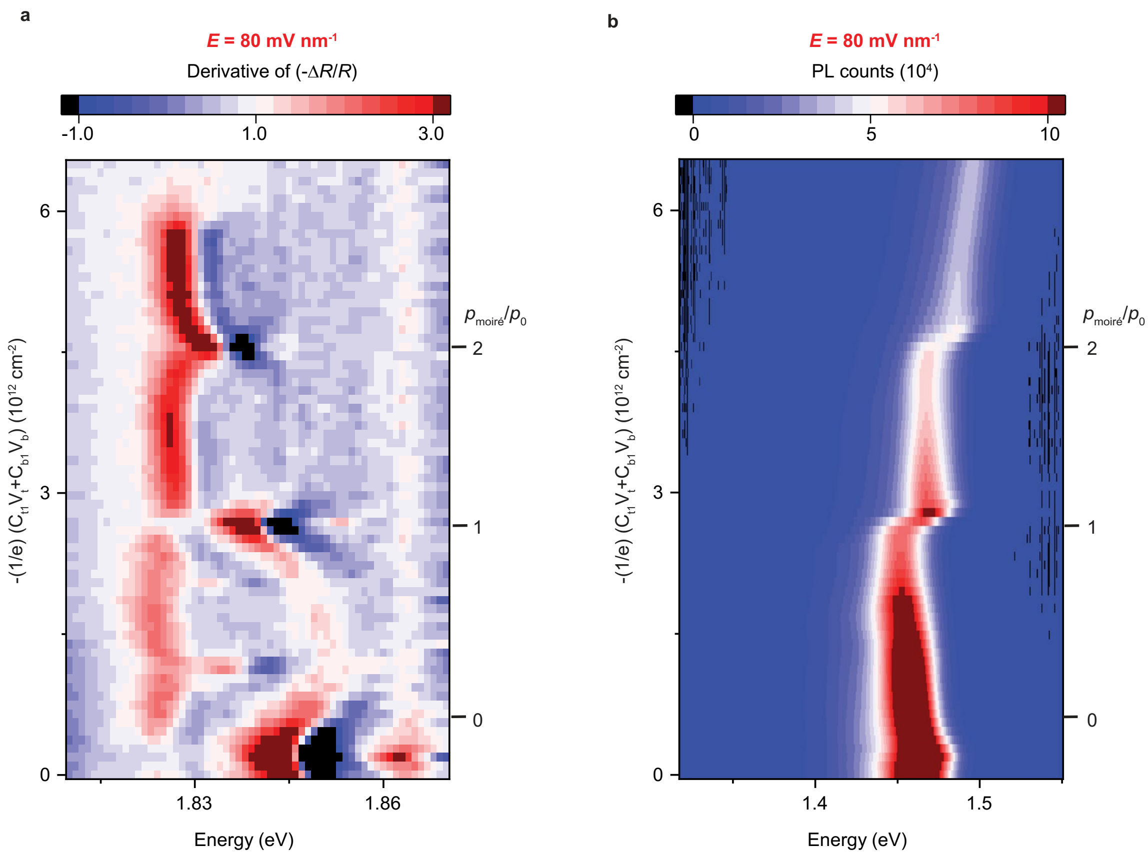

Extended Data Fig. 3 | Mott insulator state revealed by the interlayer exciton photoluminescence. a, The two-dimensional color plot of derivative reflection contrast spectra of 2s exciton at $E = 80\,\mathrm{mV\,nm^{-1}}$. Well-defined and red-shifted monolayer WSe_2 2s exciton resonances at $p/p_0 = 1$ and 2 correspond to the Mott insulator and the full filling of the moiré band (that is, two holes per moiré superlattice). **b**, The two-dimensional color plot of interlayer exciton PL spectra of the WS_2/WSe_2 moiré bilayer at $E = 80\,\mathrm{mV\,nm^{-1}}$. The PL resonance energy blueshifts suddenly, and the PL intensity exhibits a sudden increase at $p/p_0 = 1$ and 2, which is consistent with the correlated states probed by the 2s exciton spectra. Therefore, this abrupt increase of interlayer exciton PL intensity provides a reliable signature of the Mott insulating state with one hole at each moiré superlattice ($p_{moiré}/p_0 = 1$ or 2).

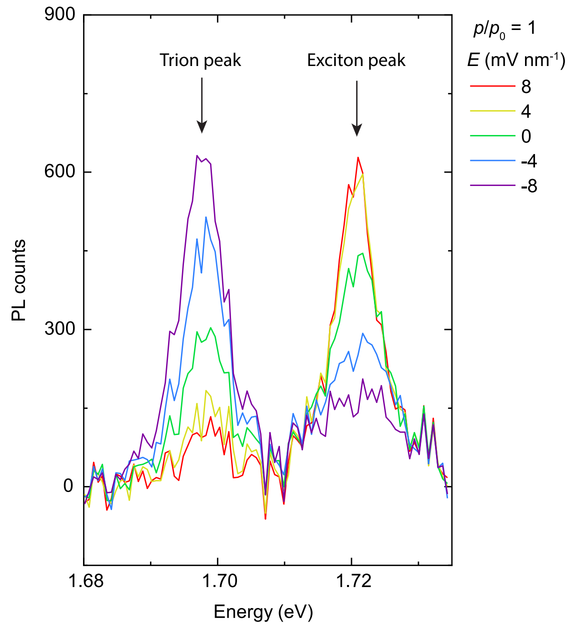

Extended Data Fig. 4 | The trion signal at different vertical electric fields in the correlated interlayer exciton insulator. The binding energy of the trion energy is around 21 meV.

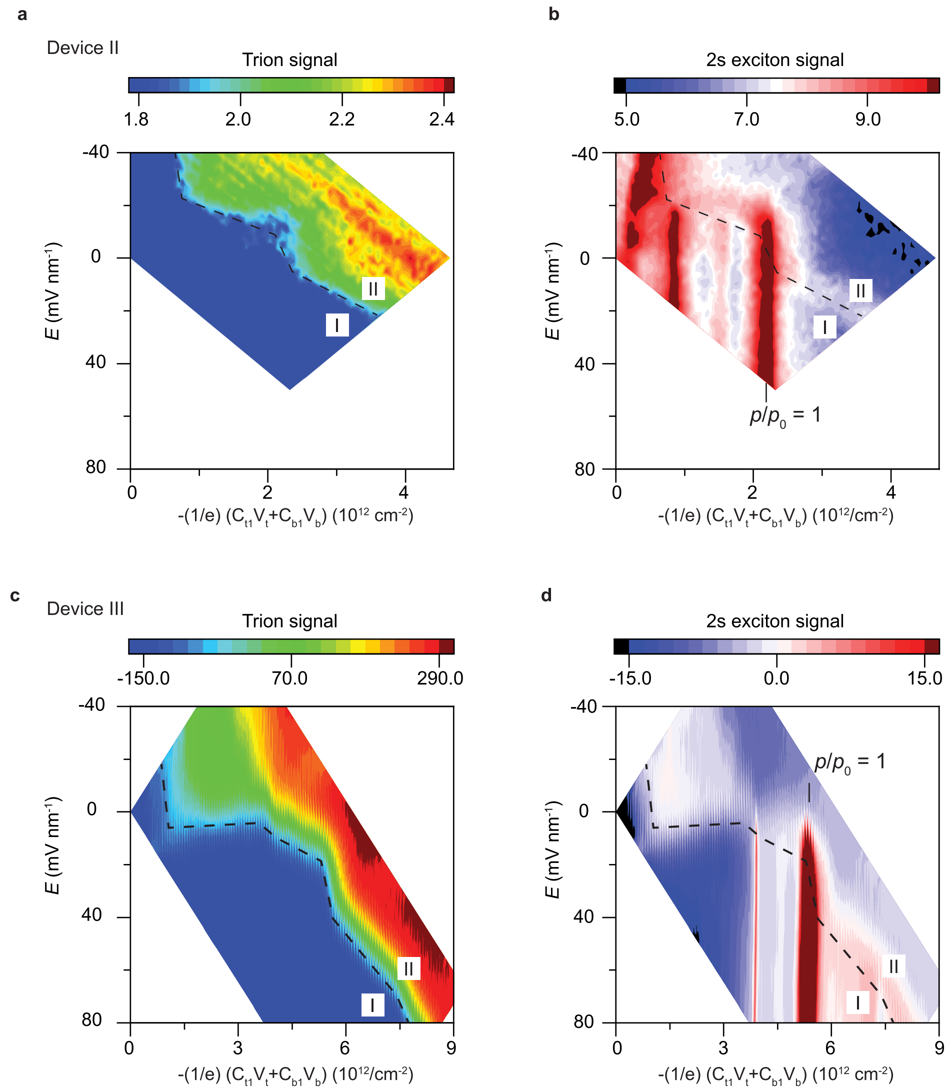

Extended Data Fig. 5 | Phase diagram of the correlated interlayer exciton insulator in device II and device III. a and **b**, The WSe_2 monolayer trion signal in the reflection contrast spectra (**a**) and WSe_2 monolayer 2s exciton signal in the derivative reflection contrast spectra (**b**) as a function of gates' induced hole density and vertical electric field *E* in device II. The dashed black line, determined by the emergence of the trion signal in **a**, separates region I (with a charge-neutral WSe_2 monolayer) from region II (with a hole-doped WSe_2 monolayer). The strongest 2s resonance at $p/p_0=1$ in the region I of **b** defines the Mott insulator state of the moiré bilayer. This Mott insulator state becomes a correlated interlayer exciton insulator as the resonance extends to region II of **b** at the combined hole density $p/p_0=(p_{moiré}+p_{mono})=1$. **c** and **d**, WSe_2 monolayer trion signal (**c**) and WSe_2 monolayer 2s exciton signal (**d**) in the derivative reflection contrast spectra function of gates' induced hole density and vertical electric field *E* in device III. The dashed black line, determined by the emergence of the trion signal in **c**, separates region I (with a charge-neutral WSe_2 monolayer) from region II (with a hole-doped WSe_2 monolayer). The strongest 2s resonance in region I of **c** defines the Mott insulator state of the moiré bilayer. This Mott insulator state also becomes an interlayer exciton insulator as the resonance extends into region II of **c** with the combined hole density $p/p_0=(p_{moiré}+p_{mono})=1$, and eventually disappears at the negative vertical electric field.

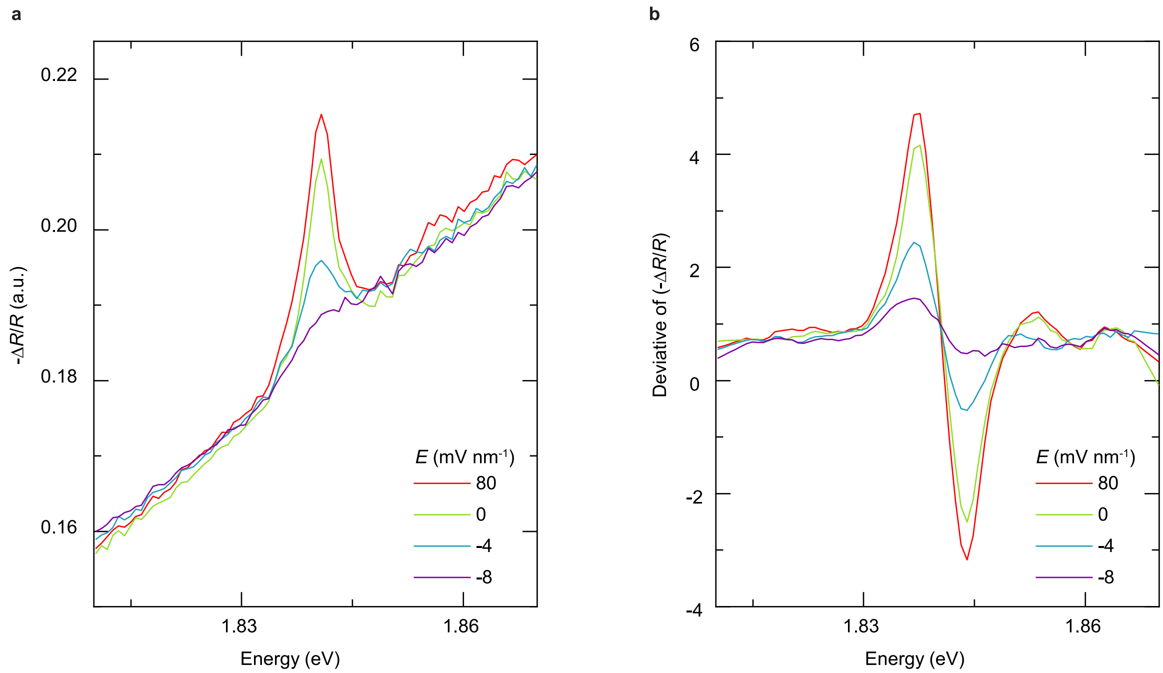

Extended Data Fig. 6 | Line cuts of 2s exciton signal in the Mott insulator and correlated interlayer exciton insulator. a, Reflection contrast spectra in the Mott insulator ($E = 80\,\mathrm{mV\,nm^{-1}}$) and correlated interlayer exciton insulator ($E = 0$, −4, and $-8\,\mathrm{mV\,nm^{-1}}$). **b**, Derivative reflection contrast spectra in the Mott insulator ($E = 80\,\mathrm{mV\,nm^{-1}}$) and correlated interlayer exciton insulator ($E = 0$, −4, and $-8\,\mathrm{mV\,nm^{-1}}$). It clearly shows that the WSe_2 2s exciton feature decreases in amplitude at $p/p_0 = 1$ with a reduced vertical electric field (increased hole doping in the WSe_2 monolayer). The WSe_2 2s exciton amplitudes of the interlayer exciton insulator states ($E = 0$, −4, and $-8\,\mathrm{mV\,nm^{-1}}$) are weaker than that of the Mott insulator ($E = 80\,\mathrm{mV\,nm^{-1}}$).

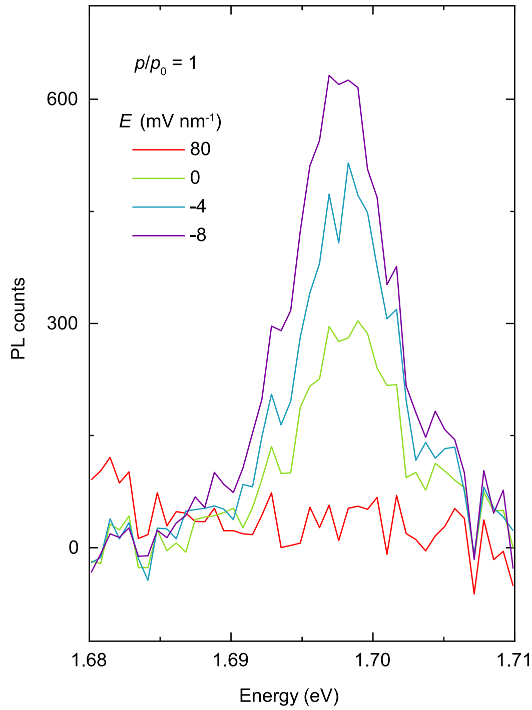

Extended Data Fig. 7 | Line cuts of trion signal in the Mott insulator and correlated interlayer exciton insulator. For the Mott insulator ($E = 80$ mV nm^{-1}), the WSe_2 monolayer does not have a trion state, while in the correlated interlayer exciton insulator state, the WSe_2 monolayer does have a trion state ($E = 0$, -4, and -8 mV nm^{-1}).

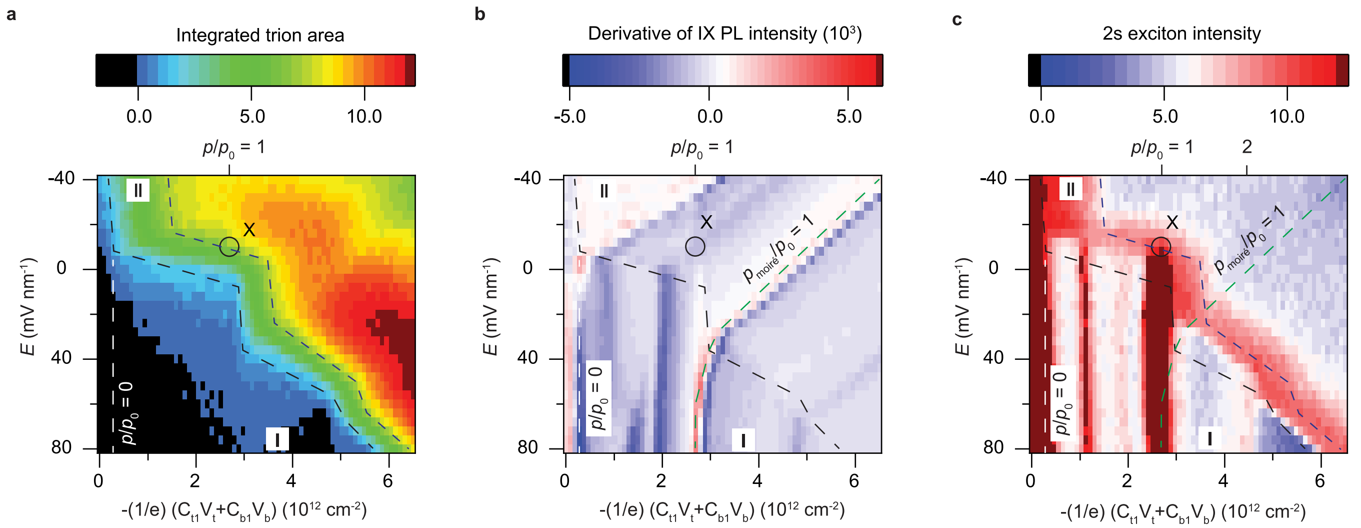

Extended Data Fig. 8 | Estimation of critical interlayer exciton density. a–c, WSe_2 monolayer trion intensity (**a**), Derivative of interlayer exciton PL intensity with respect to gates induced hole density $dI_{IX}/\left[-\frac{1}{e}\left(C_{t1}V_t + C_{b1}V_b\right)\right]$ (**b**), and WSe_2 monolayer 2s exciton intensity (**c**) as a function of the gates induced hole density $-\frac{1}{e}\left(C_{t1}V_t + C_{b1}V_b\right)$ and vertical electric field E. The same figures are plotted in Fig. 3a–c, in the main text. The critical point is labeled as point X, where the correlated interlayer exciton insulator starts to melt, as shown in **c**. The dashed black line in **a** denotes states with the same trion PL intensity as, and therefore similar p_{mono} to, the X point. The dashed green line in **b** corresponds to the Mott insulator in the moiré bilayer ($p_{moiré}/p_0 = 1$), which is determined by the maximum of $dI_{IX}/\left[-\frac{1}{e}\left(C_{t1}V_t + C_{b1}V_b\right)\right]$ in **b**. The carrier density in the WSe_2 monolayer p_{mono} along this green dashed line can be calculated as $p_{mono} = p - p_{moiré}$. The intersection of the dashed blue line and the dashed green line is around $p/p_0 = 1.5$. The hole density in the WSe_2 monolayer is $p_{mono} = p - p_{moiré} = 1.5\,p_0 - p_0 = 0.5\,p_0$ at the intersection. Point X should have a similar p_{mono} because it has the same trion intensity. Therefore, the critical interlayer exciton density at point X is $n_X = p_{mono} \approx 0.5\,p_0$.